THE JOURNAL OF PHYSICAL CHEMISTRY C
A JOURNAL OF THE AMERICAN CHEMICAL SOCIETY

pubs.acs.org/JPCC

Article

Selective Excitation of Higher Harmonic Coherent Acoustic Phonons in a Graphite Nanofilm

Arne Ungeheuer,* Ahmed S. Hassanien, Mashood T. Mir, Lukas Nöding, Thomas Baumert, and Arne Senftleben*

Cite This: J. Phys. Chem. C 2022, 126, 19822−19833

Read Online

ACCESS | Metrics & More | Article Recommendations

ABSTRACT: We investigate the excitation of higher harmonic coherent acoustic phonon (CAP) modes in a ∼42 nm thin graphite film. Results obtained from ultrafast electron diffraction (UED) measurements, employing single-pulse femtosecond-laser excitation as well as tailored double-pulse sequences to selectively drive the two first higher-order coherent acoustic phonon modes, are presented. Extracted harmonic contributions are compared and analyzed with the help of a one-dimensional kinematic diffraction model. Phase analysis is employed to discriminate higher-order frequencies found in the measured transient, which arise due to the presence of excited coherent acoustic phonon modes, from frequency contributions that are inherent to the ultrafast electron diffraction measurement principle.

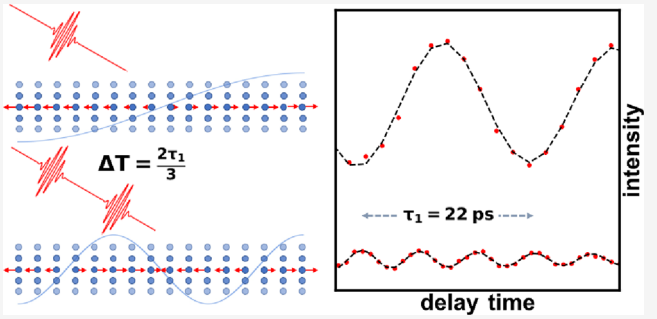

INTRODUCTION

Over the past decades, the study of femtosecond-laser-excited coherent acoustic phonons in the gigahertz to terahertz regime has attracted considerable interest and already led to the development of a wide range of applications as a versatile probing technique. In the field of picosecond ultrasonics for example, coherent strain waves excited in bulk material have been used to study the properties of buried nanostructures[1,2] and developments such as damage-free acoustic imaging of cells[3,4] or ultrafast magnetoacoustics[5,6] further demonstrate the exciting possibilities, while also underscoring the importance of the availability and development of tailored coherent acoustic phonon sources. Since the advent of two-dimensional van der Waals materials in the early 2000s, sparked by the development of the mechanical exfoliation technique (scotch tape method)[7,8] and the associated easy availability of high-quality single-crystal thin-film samples in a wide thickness range between tens of nanometers to atomic monolayers, the study of coherent acoustic phonons has also been extended to this class of materials. Several experiments have demonstrated the generation of CAPs in thin nanofilms of metals, such as gold,[9,10] bismuth,[11] and aluminum;[12] semimetals like graphite;[13] and semiconductors like MoS_2[14] WSe_2[15] GaN,[16] and others.[17,18] However, in contrast to strain waves excited in bulk material, the allowed nanomechanical longitudinal displacement fields in these ultrathin nanofilms are constricted to a series of quantized resonances, depending on the boundary conditions imposed on the system. Therefore, the amplitudes of specific modes from this series are determined by the spatiotemporal stress distribution within the sample, induced by the ultrashort laser pulse. Previous studies on freestanding silicon membranes[19] in the few-hundred-nanometer-thickness regime showed a large series of odd higher harmonics due to the large optical absorption length for the used wavelength and therefore spatially uniform excitation profile within the material. Since odd harmonics correspond to an antisymmetric displacement field and a symmetric strain field with respect to the center of the film (vice versa for even harmonics), the excitation of even modes requires a spatially non-uniform component in the photoinduced stress distribution. In agreement with this, silicon films equipped with a strongly absorbing metal transducer, resulting in a highly non-uniform excitation profile, led to the observation of additional even harmonics and, moreover, to the observation of a frequency comb in the spectral domain, corresponding to propagating strain pulses.[20]

In this contribution, we extend the study of femtosecond laser-excited higher-order CAP modes in nanomembranes to graphite as a prototypical van der Waals material and to a

Received: September 7, 2022
Revised: October 17, 2022
Published: November 16, 2022

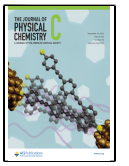

https://doi.org/10.1021/acs.jpcc.2c06401
J. Phys. Chem. C 2022, 126, 19822−19833

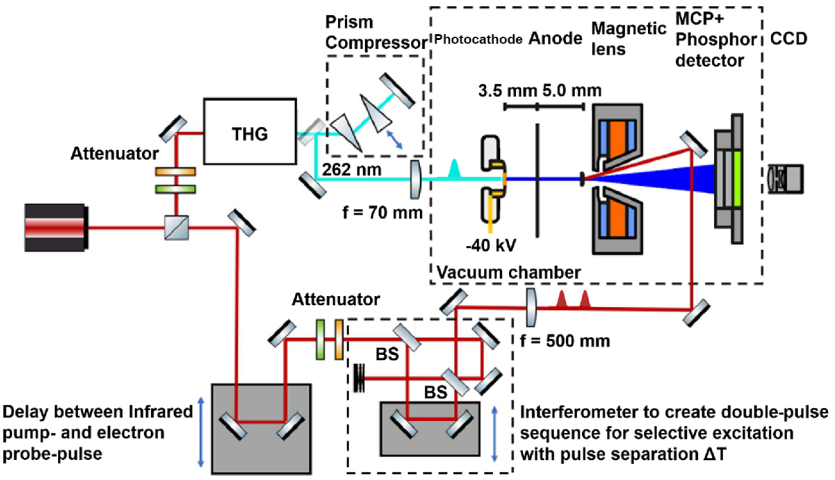

Figure 1. Schematic representation of the ultrafast electron diffraction setup. For the generation of the electron probe pulse, the third harmonic (262 nm) is first generated to extract free electrons from the photocathode. On the pump arm, a Mach−Zehnder-type interferometer is employed in order to generate double pulses with variable delay time ΔT.

thickness regime one order of magnitude smaller, corresponding to typical fundamental oscillatory periods on the timescale of a few tens of picoseconds. With the goal to coherently drive specific higher-order CAP modes, while simultaneously attenuating the dominant fundamental, we employ a double-pulse excitation scheme, with the pulse separation adjusted to yield constructive interference for the respective harmonics. We report the clear observation of a second and third harmonic CAP signal in a ∼42 nm thin, quasi-freestanding graphite membrane, which demonstrates the possibility to excite and amplify CAP harmonics selectively via multi-pulse sequences in the examined frequency regime. It should be emphasized that the excitation and observation of higher harmonics is not self-evident here, because vibrational periods are comparable to the typical duration of the photoinduced strain pulse and the coherent atomic motion could be damped or washed out completely as a result of convolution with the transient force driving the system.

Comparison of previous reports on CAPs in thinner and thicker nanofilms, e.g., for Si[19,21] and black phosphorus,[22] reveals that higher-order CAP modes are clearly present in thicker samples (few 100 nm-thickness regime), while they are absent or only faintly visible in thinner membranes (few 10 nm-thickness regime), raising the question of whether these modes can be excited and enhanced by tailored laser-pulse sequences.

A direct comparison of our single-pulse and double-pulse experiments reveals the necessity to carefully analyze the frequencies that are contained in the electron diffraction data. We propose a way to discriminate between higher-order frequencies that correspond to the actual coherent nanomechanical lattice vibrations and contributions that arise due to the measurement principle of ultrafast electron diffraction. In order to do this, the individual contributions are identified via phase analysis, derived from a one-dimensional kinematic diffraction model to describe the observed dynamics.

METHODS

Our current ultrafast electron diffraction setup,[23] utilized for the time-resolved pump−probe experiments presented here, is depicted in Figure 1. Laser pulses with a duration of 25 fs FWHM and a 785 nm central wavelength are generated by a Ti:sapphire multipass amplifier with a repetition rate of 3 kHz and up to 1.6 mJ pulse energy. Utilizing around 10% of the maximum pulse energy, the laser beam is first divided into separate pump and probe paths. On the probe arm, the fundamental is frequency-tripled in a harmonic generator (THG) by second-harmonic generation and subsequent sum-frequency generation to produce UV pulses with a central wavelength of 262 nm. After passing a prism compressor to compensate for dispersion (minimal UV laser pulse duration is estimated to be 30 fs FWHM after compensation), the UV pulses are focused on a gold photocathode (40 nm gold on a sapphire substrate with a 3 nm Ti−Cr contact layer) inside the UHV chamber, where they can emit a bunch of electrons via the linear photo effect. After acceleration to 40 keV kinetic energy over a 3.5 mm distance, the electron pulses pass through a 100 μm pinhole in the center of the grounded anode and reach the sample after an additional 5 mm field-free drift region. Using a magnetic lens, the diffracted electrons are then focused onto the detection unit, where the signal is first amplified by a chevron stack of micro-channel plates (MCP) before reaching the P43 scintillator screen from which the imaged diffraction pattern is recorded with a CCD camera. Since the time resolution of the ultrafast electron diffraction setup is mainly limited by the electron-pulse duration, the number of electrons per pulse is kept at 800−1500 electrons to limit temporal pulse broadening due to Coulomb repulsion during propagation.[23] The number of electrons can be controlled by tuning the UV output power of the harmonic generator with the help of a $\lambda/2$ waveplate and a polarizer and is measured with a Faraday cup connected to a picoampere meter that can be inserted into the electron beam path after the magnetic lens. To further optimize the performance of the experiment, the UV lens (f = 70 mm) position can be adjusted to vary the spot diameter on the gold cathode between 2 and 30 μm. Typically, around 10 μm is chosen in order to achieve a good tradeoff between spatial coherence (few nanometer) and electron pulse duration (about 200 fs).[23]

To vary the time delay between the pump laser pulse and the probe electron pulse, the pump beam first traverses a motorized delay stage. A Mach−Zehnder-type interferometer equipped with two 50/50 beam splitters (BS) in the pump beam path produces double pulses with adjustable relative time

https://doi.org/10.1021/acs.jpcc.2c06401
J. Phys. Chem. C 2022, 126, 19822−19833

delay. Using a lens with a long focal distance (f = 500 mm), the pump beam is focused onto the sample via an additional mirror inside the vacuum chamber. To ensure homogeneous optical excitation over the spatial extent of the ∼150 μm electron spot, the pump laser beam is slightly overfocused, resulting in a 480 μm (FWHM) spot diameter at sample position. A pump energy of 2.3 μJ for each pulse in the pulse pair was chosen, corresponding to a fluence of 880 μJ/cm^2 with an estimated pulse duration below 30 fs. A temporal and spatial overlap between pump and probe is achieved by observing the shadow image of a 300-mesh hexagonal TEM gold grid. The laser pulse excites a free-electron cloud above the grid surface, which acts as a diffuser and leads to a blurring effect in the grid's shadow image. Close to the temporal overlap, this blurring effect vanishes and the corresponding delay-stage position is determined for both pump pulses separately.

Figure 2 depicts examples of static diffraction patterns, recorded at a negative time delay (before arrival of the excitation pulse) for the graphite specimen used in the experiments. Figure 2a shows the diffraction pattern with the sample's surface normal (equal to the c-axis of graphite) oriented parallel to the electron beam propagation direction, while in Figure 2b, the diffraction pattern for a 33° tilt between the surface normal and the electron beam propagation direction is shown. This sample tilt is necessary to image diffraction orders that are sensitive to positional changes of lattice atoms parallel to the graphite c-axis (Miller indices (hkl) with $l \neq 0$), associated with the longitudinal coherent acoustic phonon modes.

For a thin crystalline film, the lattice points in reciprocal space turn into reciprocal lattice rods (relrods)[24] that become increasingly elongated with decreasing sample thickness. Since the experimentally observed Bragg spot intensity is related to the Ewald sphere overlap with the corresponding relrod, the spot shape and brightness strongly depend on the sample orientation and the relrod intersection point with the Ewald sphere, while the transient behavior is encoded in the time-dependent overlap due to the altered relrod distribution. In general, a thicker specimen leads to a higher CAP detection sensitivity due to the narrower peak profile in reciprocal space and a more pronounced change in the overlap between the Ewald sphere and the shifting relrod. In the experiments presented here, a specimen with ∼42 nm thickness, corresponding to 124 atomic layers (interlayer distance 0.336 nm), was chosen.

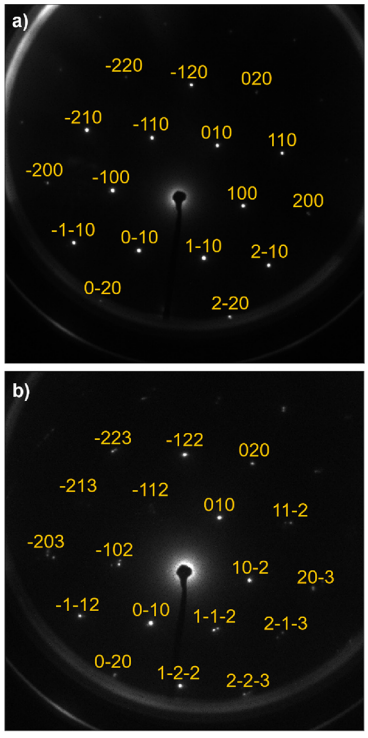

Figure 2. Transmission electron diffraction image of the examined graphite flake, obtained for normal incidence of the electron probe beam (a) and for a 33° tilted sample geometry (b), which allows the observation of higher-order diffraction spots with Miller index $l \neq 0$.

For a typical measurement, 3000 images of the diffraction pattern per delay step, each integrated over an exposure time of 200 ms, are taken and summed up to obtain a good signal-to-noise ratio. To compensate for long-time fluctuations of the experimental setup, the total number of images is divided over 60 delay-stage cycles, resulting in 50 images per cycle. A 40 pixel × 40 pixel range of interest (ROI) around the Bragg peak is selected for the evaluation. For background removal, the diffuse electron background is approximated by a two-dimensional linear plane intersecting three points at the corners of the ROI and subtracted for each Bragg spot individually. The isolated peak of elastically scattered electrons is then fitted with a pseudo-Voigt profile (Gaussian−Lorentzian sum), and the obtained amplitude is evaluated for each timestep.

Sample Preparation. The graphite sample was prepared based on the method of mechanical exfoliation introduced by Novoselov et al. and Geim et al. (scotch tape method)[7,8] as well as related variants, such as the stamping method.[25] Graphite crystals are cleaved three to eight times using commercially available transparent viscoelastic gel film based on PDMA (Gel-Pak). The gel film is searched under the optical microscope for crystal flakes of suitable lateral size (>50 μm × 50 μm) and thickness by measuring the transmitted light from a white-light source. Taking into account the complex refractive indices of graphite, air, and PDMA and employing the transfer matrix method[26] to take into account internal reflections, the thickness of the selected flakes can be determined from the transmittance. For transfer onto a standard TEM 2000 mesh copper grid, a small piece of solvable adhesive (Crystalbond 509) is melted to a dome-shaped drop on a PDMA substrate by heating for 3 min at 110 °C. Subsequently, the grid is positioned on top of the adhesive cone and bonded by heating for 2 min at 90 °C. During the heating process, the grid is carefully observed under the microscope. When a thin film of adhesive permeates through the copper mesh, the adhesive is left to cool down and solidify. The gel film with the graphite flake is then applied top-down onto the copper mesh and gently pressed to ensure good contact between the crystal flake and the adhesive layer. Another short heating step at 90 °C for 30 s is applied to attach the crystal to the adhesive, and after cooling down, the gel film is slowly peeled off, leaving the graphite flake on the adhesive layer due to the much stronger retention. Now the PDMA substrate is stripped off as well and the dome of the adhesive is thoroughly embedded in filter paper, leaving the top with the copper grid and sample uncovered. By applying acetone onto the filter paper several times, the Crystalbond is slowly dissolved, yielding a quasi-freestanding graphite flake on

https://doi.org/10.1021/acs.jpcc.2c06401
J. Phys. Chem. C 2022, 126, 19822−19833

the copper mesh. Figure 3 shows the transferred graphite flake on the TEM grid in reflection and transmission under the optical microscope, for which the evaluation of the transmittance yields a film thickness of ∼42 nm. It can be seen in the reflection image that the relaxation of the graphite membrane onto the supporting mesh-grid structure results in a slightly wavy sample geometry and a slight bulging of the specimen at each individual mesh hole. A possible influence of this bulging on the observed CAP dynamics in the UED measurements is discussed in the numerical analysis.

RESULTS AND DISCUSSION

Single-Pulse and Double-Pulse Excitation of Coherent Acoustic Phonons. In order to investigate the possibilities to excite higher-order coherent acoustic phonon modes in ultrathin graphite nanofilms, pump−probe experiments using single laser pulses as well as double-pulse sequences for excitation have been performed. The total absorbed energy was kept identical in each case, with a pulse energy of 4.6 μJ used for single-pulse excitation and 2.3 μJ for each pulse in the double-pulse sequence, respectively. Figure 4a exemplarily shows the transient intensity for the (2 0−3) Bragg peak after single-pulse excitation over a pump−probe delay window ranging from −40 to 80 ps, obtained in a 33° tilted sample geometry. For all traces, the data is presented relative to the averaged intensity at negative time delays. In the main plot of Figure 4a, the fitted peak amplitude is displayed, while the inset shows the decomposition of the transient into its frequency components after baseline subtraction. This baseline is assumed to contain a rocking-curve contribution[27] due to the increased equilibrium lattice constant in the laser-heated sample, as well as a contribution originating from the Debye−Waller effect.[28] While the Debye−Waller effect always results in a decreased Bragg peak intensity after sample heating, the contribution due to the altered lattice constant can lead to either an increase or a decrease, depending on the exact sample alignment with respect to the electron-beam propagation direction. To include both, a biexponential behavior was assumed and fitted together with a series of decaying sinusoids to take into account the oscillatory behavior originating from the fundamental CAP mode, as well as higher-order contributions. The resulting function is

$$I_{\mathrm{Fit}}(t) = \begin{cases} 1, & t < 0 \\ 1 + a_1\left(e^{-\frac{(t-t_0)}{\delta_1}} - 1\right) + a_2\left(e^{-\frac{(t-t_0)}{\delta_2}} - 1\right) \\ \quad + \sum_n A_n e^{-\frac{(t-t_0)}{\tau_n}} \sin(2\pi n f_1 (t - t_0) + \phi_n), & t \geq t_0 \end{cases} \tag{1}$$

Here, t_0 denotes the arrival time of the last excitation pulse, $\delta_{1,2}$ and $a_{1,2}$ characterize the timescales and amplitudes of the biexponential decay, and τ_n is the decay rate for the oscillating component with frequency nf_1, with corresponding phase ϕ_n and amplitude A_n. In order to extract and visualize the individual frequencies contained in the data, as shown in the inset of Figure 4a−c, the fitted function was subsequently subtracted from the measured trace, with the sinusoid corresponding to the mode of interest excluded:

$$I_{f_n}(t) = I_{\mathrm{Exp}}(t) - I_{\mathrm{Fit}}(t)|_{A_n=0} \tag{2}$$

A frequency f_1 = 46 GHz, corresponding to τ_1 = 21.8 ps periodicity, was found for the dominant, large-amplitude oscillation. This result is in good agreement with the frequency $f_{1,\,\mathrm{optical}}$ = 49 GHz of the fundamental breathing mode, obtained from the optically determined sample thickness d, employing the following relation:[29]

$$f_n = n\frac{v}{2d},\ n = 1 \tag{3}$$

where v is the sound velocity in the crystal's out-of-plane direction ($v_{\mathrm{Graphite}} = 4.14\frac{\mathrm{km}}{\mathrm{s}}$).[30] Here, eq 3 describes the resonance frequencies for a one-dimensional freestanding nanomechanical resonator model of the membrane, with stress-free boundary conditions employed at the top and bottom surfaces.

To further improve the signal-to-noise ratio of the extracted frequencies, the decomposition was evaluated for five individual Bragg peaks from the $l = \pm 2$ and $l = \pm 3$ families in the way described above and averaged subsequently (Figure 4d). Averaging is justified here since the phases of extracted frequency components from different Bragg spots were found to be almost identical. This is apart from an arbitrary 180° phase shift (corresponding to an amplitude sign change) depending on the intersection point between the Ewald sphere and the relrod profile (see also the Numerical Analysis section). To take this into account, sign matching was applied prior to averaging. It should be noted that the amplitudes obtained for the individual frequencies must be interpreted with some caution, since they not only depend on the Bragg order but also critically depend on the exact relrod intersection point with the Ewald sphere, which is related to the q_z-dependent slope of the respective overlap integral with changing mean interatomic distance. Furthermore, as described in the Numerical Analysis section, the Bragg peak intensity modulation associated with the higher-order CAP

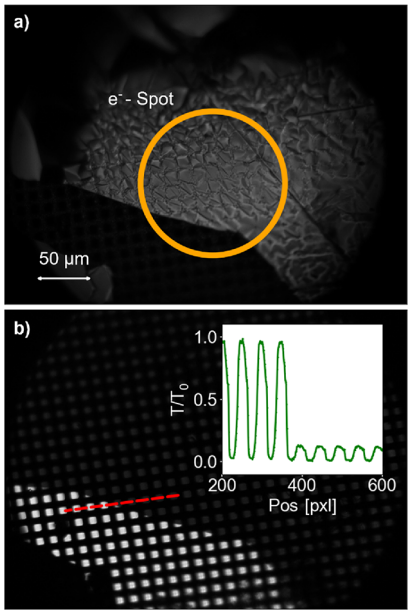

Figure 3. (a) White-light reflection image of the quasi-freestanding ∼42 nm graphite sample after transfer onto a 2000-mesh copper TEM grid. The most even sample area indicated by the orange circle was used for the UED experiments. (b) White-light transmission image for the optical estimation of the sample thickness. The inset shows the transmitted intensity along the dashed red line.

https://doi.org/10.1021/acs.jpcc.2c06401
J. Phys. Chem. C 2022, 126, 19822−19833

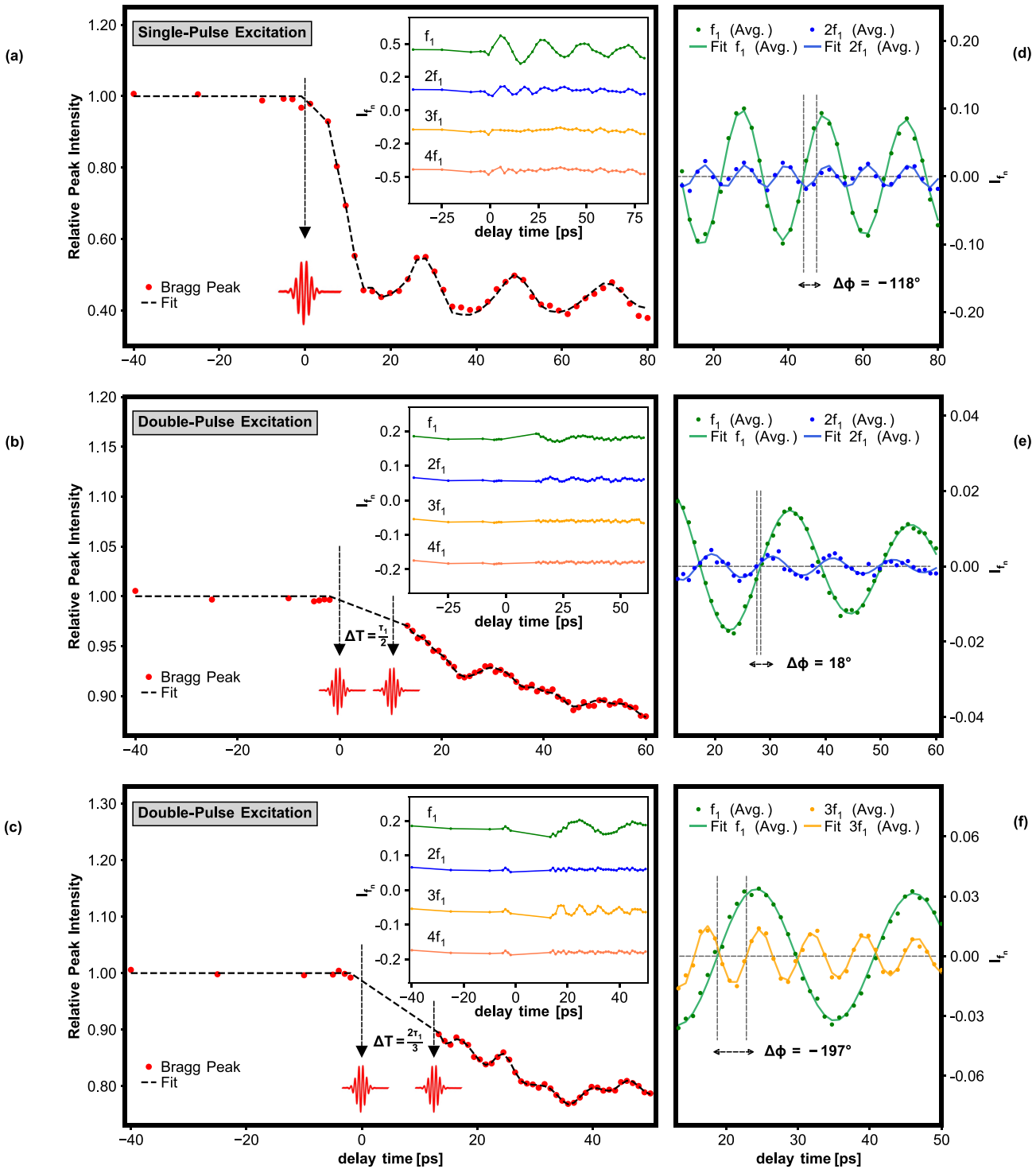

Figure 4. Excitation of longitudinal coherent acoustic phonon modes in graphite: relative transient intensity of exemplary Bragg spots after (a) single-pulse excitation, (b) double-pulse excitation in constructive interference with the second harmonic CAP mode, and (c) double-pulse excitation in constructive interference with the third harmonic CAP mode. The insets show the decomposition of the oscillatory part into multiples of the fundamental frequency f_1. (d–f) Averaged non-zero frequency components from five individual Bragg spots. The phase of the higher-order frequency component with respect to the fundamental is indicated.

modes can differ significantly as well, in particular also for the case that identical amplitudes of the corresponding atomic-displacement fields are assumed.

Besides the dominant fundamental f_1, the single-pulse measurement displays a clear higher-order contribution with frequency $2f_1$. The minor intensity fluctuations that are visible in the extracted $3f_1$ and $4f_1$ traces are found to be non-periodic and therefore attributed to noise. A direct comparison of the extracted $2f_1$ component with the fundamental trace reveals a relative phase of −118° (calculated from the time shift with respect to the fundamental and taking into account the frequency of the higher-order $2f_1$ component). As further discussed in the Numerical Analysis section, the relative phases between measured frequency contributions can be used as a

https://doi.org/10.1021/acs.jpcc.2c06401
J. Phys. Chem. C 2022, 126, 19822−19833

tool to discriminate between higher-order frequencies in the data, which originate from the excited CAP harmonics, and frequency contributions that must be attributed to effects inherent to the UED measurement technique. For example, in case of the dominant fundamental CAP breathing mode, the relrods are undergoing a comparatively strong shift in reciprocal space, which can result in nonlinear changes in the Ewald sphere overlap integral, therefore possibly leading to the appearance of higher-order frequencies in the evaluated transient. From the Numerical Analysis section, it can be inferred that for the $2f_1$ intensity modulation, which is to be assigned to the second harmonic CAP mode, a relative phase of either 0 or 180° with respect to the fundamental is to be expected. For the $2f_1$ signal originating from the nonlinear overlap change due to the presence of the fundamental breathing mode, on the other hand, a phase shift of +90 or −90° should be observed. With the measured phase shift tending more toward −90°, the $2f_1$ component in the single-pulse measurement is assumed to predominantly originate from the nonlinear overlap change, but a superimposed contribution from the second-order CAP mode possibly exists as well, leading to the observed deviation.

Therefore, to more reliably determine the presence or absence of specific higher-order CAP modes, we performed double-pulse experiments in constructive interference with the second and third harmonics, by tuning the relative time-delay ΔT in the double-pulse sequence accordingly. Constructive interference with the second harmonic for $\Delta T = \frac{1}{2}\tau_1$ is expected to result in amplification of the second harmonic and simultaneous annihilation of the fundamental under perfect conditions. Similarly, for $\Delta T = \frac{2}{3}\tau_1$, amplification of the third harmonic is expected, while the fundamental is strongly attenuated at the same time. Our choice of $\Delta T = \frac{2}{3}\tau_1$ instead of $\Delta T = \frac{1}{3}\tau_1$ was made to ensure that the relaxation of the excited electronic system into a new equilibrium state with the lattice is nearly completed before arrival of the second laser pulse. The application of this excitation scheme is expected to result in a considerably higher sensitivity to the weak higher-order CAP modes, due to the strongly attenuated fundamental and therefore much less pronounced nonlinear effects that are superimposed on the relevant measurement signal.

For both double-pulse experiments performed, the measurement was first taken with the second laser pulse blocked, in order to verify successful excitation and detection of the strong fundamental CAP mode. This measurement was then directly followed by the double-pulse excitation scheme, with the second laser pulse in the Mach−Zehnder interferometer unblocked. Figure 4b exemplarily shows the evaluated intensity transient for the (1 −2 −2) Bragg peak after double-pulse excitation in constructive interference with the second harmonic, depicting the typical observed dynamics in this measurement for Bragg orders with $l \neq 0$. The inset with the decomposed oscillatory part displays an almost vanishing fundamental due to destructive interference, with the weak remaining residual probably explained by experimental imperfections. Additionally, a clearly visible $2f_1$ contribution is found, for which further analysis of the averaged traces (Figure 4e) reveals a relative phase $\Delta\Phi = 18°$ with respect to the fundamental, close to the expected phase relationship for the second-order CAP mode, obtained from the numerical analysis under the assumption of a small asymmetric lattice distortion (see Numerical Analysis). No additional third- or fourth-order frequency contribution was identified in this measurement.

In case of the double-pulse experiment with the relative pulse delay set to $\Delta T = \frac{2}{3}\tau_1$ (Figure 4c), adjusted for constructive interference with the third harmonic CAP mode, a larger residual of the fundamental is observed, which is to be expected due to the less perfect condition for destructive interference. While no significant second harmonic contribution was found in this measurement, a comparatively strong signature of the third harmonic mode was identified, with the relative phase $\Delta\Phi = -197°$, obtained from the fitted averaged trace (Figure 4f), close to the expected phase from the numerical analysis.

Mechanisms of Driving Coherent Acoustic Phonons. The measurements presented in the previous section demonstrate the excitation of a strong fundamental CAP mode after single-pulse excitation in the graphite nanofilm. For the double-pulse experiment performed in constructive interference with the second harmonic, a clear signature of the targeted second-order CAP mode is observed, together with a weak remaining residual of the fundamental. In the case of the double-pulse experiment adjusted for constructive interference with the third harmonic, a comparatively strong contribution from the targeted third-order CAP mode was extracted from the transient in superposition with the attenuated fundamental. No significant contribution of the second-order CAP mode was visible in this case.

To further discuss the experimental findings and its implications, we consider the usual formalism for the description of longitudinal coherent acoustic phonons in a spatially constricted system. For a laser beam diameter much larger than the heat penetration depth, generation and propagation of longitudinal coherent acoustic phonons is described by the one-dimensional inhomogeneous wave equation, with the gradient of the photoinduced spatiotemporal stress distribution $\sigma(z, t)$ acting as the source term:[31,32]

$$\frac{\partial^2 u(z,t)}{\partial t^2} - v^2 \frac{\partial^2 u(z,t)}{\partial z^2} = \frac{1}{\rho}\frac{\partial \sigma(z,t)}{\partial z} \tag{4}$$

Here, $u(z, t)$ is the lattice displacement parallel to the CAP propagation direction, v is the sound velocity, and ρ is the mass density of the considered medium. In the case of a freestanding film, stress-free boundary conditions $\rho v^2 \frac{\partial u}{\partial z} + \sigma = 0$ at $z = 0, d$ are imposed at the open ends of the nanomechanical resonator.[31,32] Steady-state solutions to this equation can be described as a superposition of standing waves of the following form:[33]

$$u(z,t) = \sum_n A_n \cos\left(\frac{n\pi}{d} z\right) \sin(2\pi n f_1 \times t + \phi_n) \tag{5}$$

with the frequency of the fundamental mode f_1 given by the time the acoustic wave takes to travel back and forth within the thin film (see eq 3).

The two most relevant physical mechanisms in a non-piezoelectric material that lead to a photoinduced mechanical stress after femtosecond laser excitation are thermoelastic stress σ_{TE} and the deformation potential σ_{DP}. The mechanical stress related to the deformation potential mechanism originates from the modified energetic distribution of the electronic system after absorption of the optical excitation

https://doi.org/10.1021/acs.jpcc.2c06401
J. Phys. Chem. C 2022, 126, 19822−19833

pulse, which results in altered interatomic forces and thus a change in the atomic equilibrium position. While a rigorous treatment of the deformation-potential mechanism requires inclusion of the material's band structure and consideration of the occupation of specific energy levels, a simplified description for a metal can be derived from the electronic pressure:[31,32]

$$\sigma_{\mathrm{DP}}(z, t) = -\gamma_{\mathrm{e}} c_{\mathrm{e}} \delta T_{\mathrm{e}}(z, t) \tag{6}$$

Within this approximation, the spatiotemporal stress in the material is directly proportional to changes in the electronic temperature δT_{e}, scaled by the material-specific electronic heat capacity c_{e} as well as the electronic Grüneisen coefficient γ_{e}.

The photoinduced thermoelastic stress on the other hand is linked to the effect of thermal expansion. When photoexcited carriers are scattered by the lattice atoms, they release some of their energy in the form of thermal phonons, resulting in an increased local lattice temperature. This temperature rise is then linked to an increased thermoelastic pressure and corresponding thermoelastic stress, proportional to the change in lattice temperature δT_{L}:[31,32]

$$\sigma_{\mathrm{TE}}(z, t) = -\gamma_{\mathrm{L}} c_{\mathrm{L}} \delta T_{\mathrm{L}}(z, t) \tag{7}$$

where γ_{L} is the lattice Grüneisen coefficient and c_{L} is the lattice heat capacity, directly connecting the induced thermoelastic stress with the increase in lattice temperature δT_{L}.

In a simplified description, the spatiotemporal electronic and lattice temperatures T_{e}, T_{L} can be modeled for a given laser pulse envelope by a two-temperature model (TTM).[34] Within this model, the two systems are regarded as separate heat reservoirs, characterized by their temperature-dependent heat capacities c_{e}, c_{L} and heat conductivities κ_{e}, κ_{L}, with the heat transfer between electrons and lattice taken into account by a coupling constant g_{eL}. Unfortunately, it was not feasible at this point to determine a meaningful estimate of the temperature equilibration dynamics in graphite within the framework of the TTM, due to a lack of experimental and theoretical data for the T_{e}-dependent electronic out-of-plane heat conductivity κ_{e}. Moreover, previous studies have shown that the Wiedemann–Franz law is not applicable as an approximate description.[35]

However, we can make the following considerations: Directly after the optical excitation process, carriers typically thermalize on a timescale of less than 150 fs.[36−38] The Lambert–Beer-type behavior in a strong absorber like graphite initially leads to a highly nonuniform electronic temperature profile with a steep gradient in the crystal's out-of-plane direction. Immediately afterward, heat diffusion within the electronic system, as well as heat transfer to the lattice, starts to take place, until a thermal equilibrium between electrons and lattice is established over the spatial extent of the sample. The timescale of this equilibration process and the coupling dynamics to the lattice are therefore directly linked to the time-dependent stress distribution and the associated spectrum of driven CAP harmonics.

For instance, if one assumes a nearly instantaneous thermal diffusion process on a timescale that is very short compared to the phonon periodicities involved, this corresponds to the case of a rectangular, spatially uniform stress profile. In this case, only the odd-order harmonics, associated with an antisymmetric displacement field $u(z, t)$ (with respect to the center of the nanofilm) and symmetric strain field $\frac{\partial u}{\partial z}$ correspondingly, are driven by the photogenerated stress.[20] This selectivity can be understood by looking at the projection of the respective CAP harmonic strain field onto the photoinduced stress distribution, which is non-vanishing only for the odd modes. On the other hand, the excitation of even-order harmonics, associated with an antisymmetric strain field, requires a considerable asymmetry in the photogenerated stress. Therefore, assuming an exponential decay in the out-of-plane stress profile due to a longer thermal equilibration time would result in a non-vanishing overlap with the strain field of even-order modes.

From these considerations, we conclude that the experimental observation of a second harmonic contribution in the double-pulse measurement performed for $\Delta T_{\mathrm{rel}} = \frac{\tau_1}{2}$ indicates that the assumption of uniform heating in the ∼42 nm graphite nanofilm is not valid. Even though a quantitative inference of the precise photoinduced stress profile is not feasible due to the unknown exact intersection point of the Ewald sphere with the relrod profile, upon which the measured amplitudes of the CAP modes depend (see Numerical Analysis), we conclude that the photoinduced spatiotemporal stress profile in the graphite film must retain a significant antisymmetric part to allow for the excitation of the second-order CAP mode. On the other hand, the observation of a comparatively strong third harmonic in the double-pulse experiment with $\Delta T = \frac{2\tau_1}{3}$ is attributed to the overlap with the symmetric part of the stress distribution.

The sine-type temporal dependency of the CAP modes specified in eq 5 reflects the assumed impulsive nature of the CAP excitation process in the graphite nanofilm. This assumption is justified by the observed sine-like oscillatory behavior of the fundamental CAP mode extracted from the single-pulse measurement (see inset of Figure 4a).[39] Previous terahertz spectroscopy studies on graphite have shown that more than 90% of the excitation energy absorbed by the electronic system is transferred to the lattice within a 500 fs time span.[40] This is also supported by UED measurements of the Debye–Waller effect in graphite, which revealed a biexponential Bragg peak intensity decay with a fast component on a timescale of 700 fs or below, which is attributed to the relaxation of hot carriers to strongly coupled optical phonons (SCOPs).[13,28] A slower decay component on a 10 ps timescale is mainly attributed to the subsequent lattice thermalization due to cooling of the SCOPs via phonon–phonon scattering.[13,28] In agreement with this, the observed shift of radial Bragg peak positions (indicating thermal expansion) in our measurements was found to be on the same timescale. The rapid drop in electronic temperature resulting from the heat transfer to the SCOPs (on a timescale very short compared to the CAP periodicities considered in this work) therefore gives rise to an impulsive excitation of CAPs via the deformation potential mechanism. If, on the other hand, one would assume a significant superimposed contribution from thermoelastic stress, related to the corresponding rise in lattice temperature, this would lead to a considerable phase shift in the measurement. We therefore conclude that the dominant CAP excitation mechanism in the graphite membrane is the deformation potential mechanism. Furthermore, this implies that for the double-pulse experiments, it can be assumed that the first photoinduced stress pulse has completely decayed at the arrival time of the second laser pulse. Nevertheless, it should be mentioned that a small influence of a not fully completed lattice thermalization on the generation of the second stress pulse is possible and could, for

https://doi.org/10.1021/acs.jpcc.2c06401
J. Phys. Chem. C 2022, 126, 19822−19833

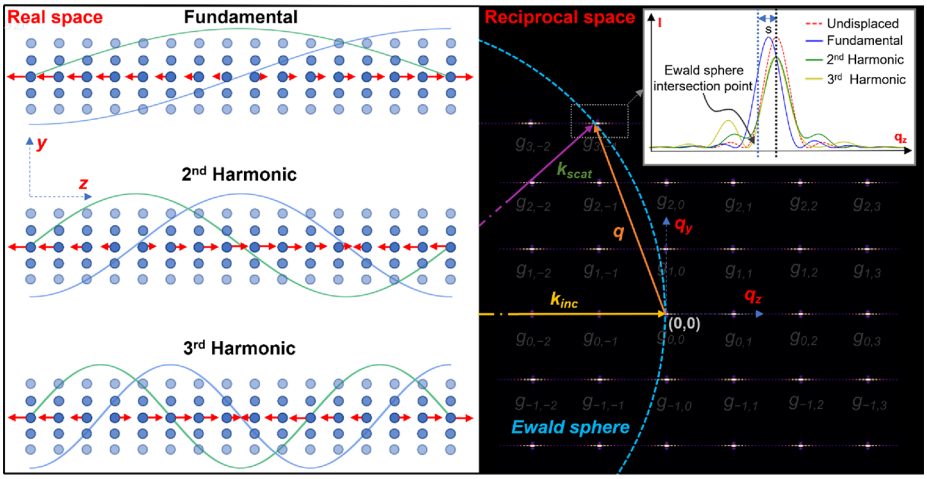

Figure 5. Schematic illustration of the CAP measurement principle using ultrafast electron diffraction: On the left, the atomic displacement field (blue) and corresponding strain field (green) is sketched for the fundamental, second harmonic, and third harmonic CAP modes. The displacement of individual atoms is indicated by red arrows. Odd harmonics correspond to an antisymmetric displacement field and symmetric strain field with respect to the center of the specimen (vice versa for even harmonics). The intersection of the Ewald sphere with the relrods in reciprocal space is sketched on the right-hand side. The time-dependent modulation of the relrod distribution in the presence of the excited CAP modes leads to a variation in the overlap between Ewald sphere and relrod that is detected in the experiment. The change in relrod distribution associated with the fundamental and first two higher harmonic CAP modes is displayed in the inset on the right for the q_z direction. The relative change is exaggerated here to illustrate the effect of individual CAP modes on the relrods more clearly. The inset shows a snapshot of the relrod distribution at the time when the atomic displacement is at its maximum. As reference, the sinc^2-type relrod profile that corresponds to the undisplaced atomic chain is plotted here as well (red dashed line). In presence of the fundamental CAP mode, the sinc^2-type relrod profile is essentially preserved, but due to the altered average interatomic distance (for odd modes, associated with an antisymmetric displacement field), the center of the relrod distribution undergoes a shift in reciprocal space, relative to the fixed Ewald sphere. In case of the second harmonic CAP mode (associated with a symmetric displacement field), the average interatomic distance remains unchanged; therefore, the center of the relrod profile is not shifted in reciprocal space. Nevertheless, the presence of the atomic displacement field leads to a redistribution of the relrod profile, which could be described as a compressed sinc^2 profile. In the case of the third harmonic CAP mode (associated with an antisymmetric displacement field and therefore altered mean interatomic distance), the presence of the displacement field leads to a strong deviation from the sinc^2-type relrod profile with a pronounced side peak, while the central peak shifts significantly less compared to the fundamental mode. The central area of the altered relrod distributions, which is experimentally most relevant, is additionally plotted in Figure 7d.

example, contribute to the imperfect cancellation of the fundamental CAP mode in the double-pulse experiment with $\Delta T = \frac{1}{2}\tau_1$.

Numerical Analysis. In general, when a CAP mode is excited in the specimen, the corresponding atomic displacement field leads to a time-dependent change in the relrod distribution in reciprocal space. This is illustrated schematically in Figure 5 for the fundamental, second harmonic, and third harmonic CAP mode, with the atomic displacement field shown on the left-hand side, while the corresponding altered relrod distribution is displayed in the inset on the right-hand side. In the UED experiment, however, the time-dependent relrod distribution is probed only at the intersection point with the fixed Ewald sphere,[41] which is then reflected in a periodic modulation of the measured Bragg peak amplitude. For a typical intersection point close to the center of the relrod, Figure 6 shows the calculated intensity modulation for a Bragg peak with Miller index $l = 2$ for the case that the fundamental, second harmonic, or third harmonic CAP mode is active in the membrane.

Since the observed intensity at the intersection point does not change linearly with the time-dependent amplitude of the atomic displacement field, higher-order frequency contributions are to be expected in the measured transient besides the actual atomic vibrational frequency. The observed frequency spectrum in a UED experiment therefore depends not only on the excited CAP modes but also on the mode-specific modulations at the Ewald-sphere intersection point. For the case that only the fundamental mode is active in the specimen, Figure 6a shows the decomposition of the calculated transient diffracted intensity into its individual frequency components. It becomes clear that beside the fundamental frequency f_1, a significant higher-order contribution with frequency $2f_1$ is contained in the transient as well. The occurrence of this higher-order frequency contribution is therefore solely due to the measurement principle of the UED technique and must be distinguished from the excitation and observation of the second-order CAP mode. As explained later in this section, it plays a critical role for the appearance of specific frequencies (in particular for the case of the second harmonic CAP mode) whether a perfect crystal lattice is assumed or whether the possibility of a small lattice distortion is considered in the numerical analysis. Figure 6 directly compares these two cases in the first and second half-periods for the respective CAP modes. Figure 7 shows the generalized numerical analysis of the intensity modulation as a function of the relrod intersection point for the fundamental, second harmonic, and third harmonic CAP modes. In addition to the amplitude, the extracted phase of the different frequency components is shown here as well. This phase information is used in the further discussion as a tool to discriminate between frequencies in the experimental data that correspond to higher-order CAP modes and higher-order frequencies that arise due to the UED measurement principle.

For the numerical analysis, we adopt a simple one-dimensional kinematic elastic diffraction model of the graphite

https://doi.org/10.1021/acs.jpcc.2c06401
J. Phys. Chem. C 2022, 126, 19822−19833

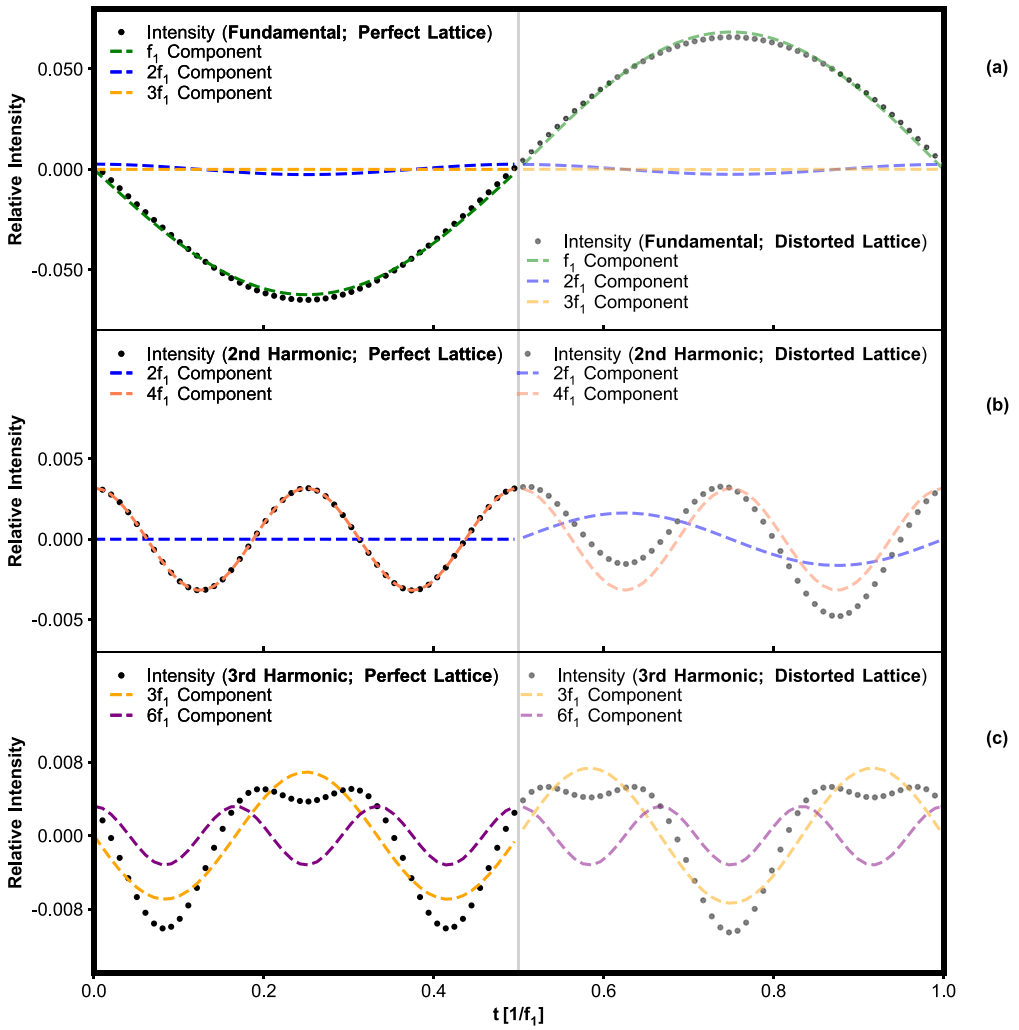

Figure 6. Elastic scattering intensity modulation calculated for the (a) fundamental, (b) second harmonic, and (c) third harmonic CAP modes employing a one-dimensional diffraction model (eq 8). The exemplary q_z value was chosen close to the relrod center to reflect typical experimental conditions. The decomposition of the obtained transients into multiples of the fundamental frequency f_1 is shown for the case of a perfect crystal lattice (first half-period) and under the assumption of a small asymmetric lattice distortion (second half-period).

film,[41] since the relevant dynamics are predominantly determined by the relrod modulation parallel to the crystals out-of-plane direction. Assuming an atomic chain with $N = 125$ atoms at positions $z_j = j \times a$, separated by the lattice constant a, we take into account the time-dependent displacement field $u_n(z_j, t)$ for the fundamental, second harmonic, and third harmonic CAP modes and calculate the transient diffracted intensity as a function of the scattering wavenumber $q_z = G_2 + s$ in the vicinity of the reciprocal lattice vector G_2. Here, the parameter s denotes the deviation from the Bragg peak center $q_z = G_2$.

$$I_n(q_z, t) \propto \left| \sum_j e^{-iq_z(z_j + u_n(z_j,t))} \right|^2 \tag{8}$$

The displacement field amplitude of the fundamental mode was approximated to $0.01 \times a$ to roughly match the experimentally observed intensity modulation. Since the degree of lattice distortion as well as the antisymmetric component of the photoinduced stress is unknown, we assumed the same displacement amplitude for the second and third harmonics within the scope of this qualitative analysis. This choice also allows for a more direct comparison of the sensitivity of the UED measurement technique with respect to the different CAP modes.

In case of the odd-order fundamental mode, the intensity modulation originates predominantly from the relrod shift in the q_z direction relative to the Ewald sphere (compare Figure 7d), which is related to the altered average interatomic distance for antisymmetric atomic displacement. The shifting intersection point with the sinc^2-type relrod profile then leads to the appearance of a significant higher-order $2f_1$ frequency contribution in the observed transient, which shows a 90° phase shift with respect to the dominant fundamental frequency f_1 (Figure 6a). As displayed in Figure 7a, this phase relation holds independent of the intersection point q_z except for a factor ±1. It is noteworthy that the analysis shows a strong q_z dependency for the relative amplitudes of the f_1 and $2f_1$ frequency components, with a vanishing amplitude of the fundamental frequency at the Bragg peak center $q_z = G_2$.

The corresponding analysis for the third harmonic CAP mode leads to similar results. Apart from the dominant $3f_1$ frequency component, a higher-order contribution with frequency $6f_1$ appears in the decomposition of the calculated

https://doi.org/10.1021/acs.jpcc.2c06401
J. Phys. Chem. C 2022, 126, 19822−19833

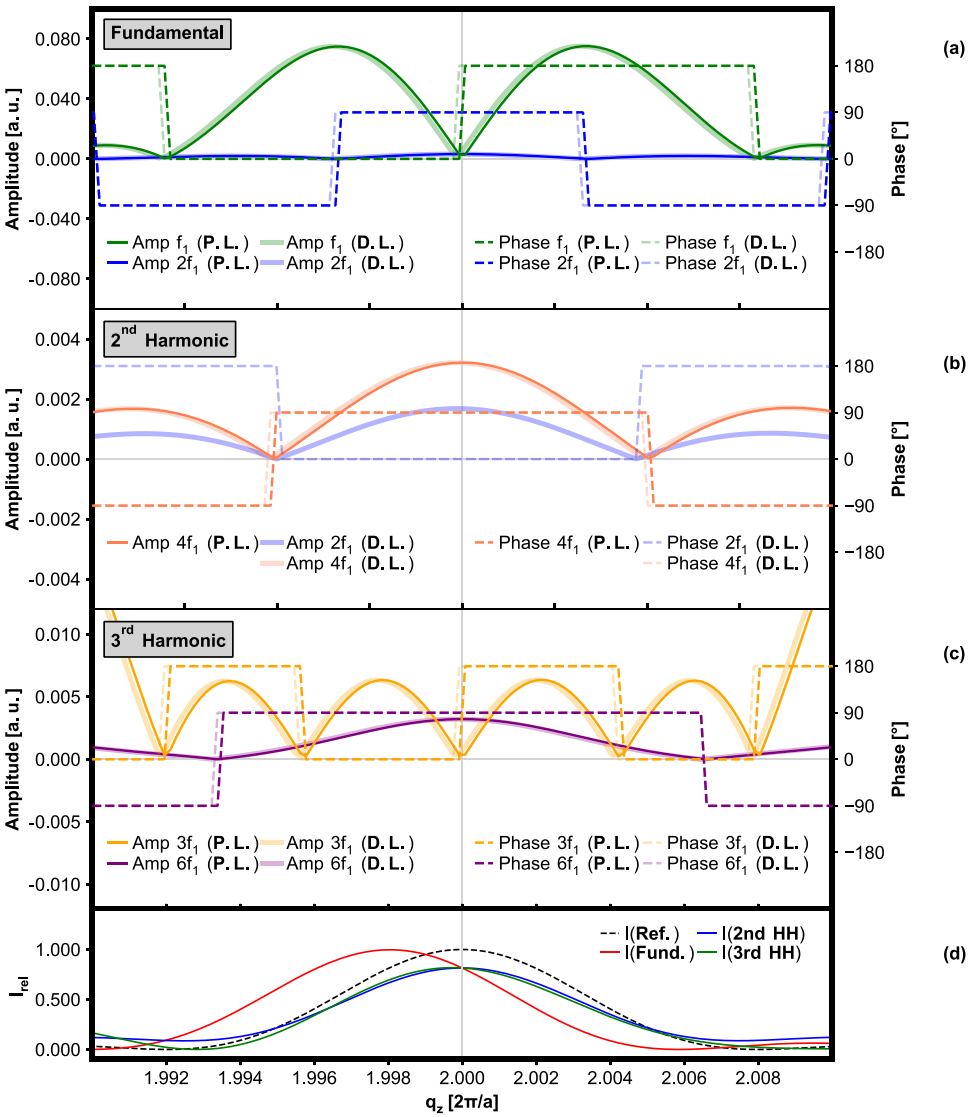

Figure 7. Amplitude and phase of the frequency components that are contained in the calculated transient relrod distribution, plotted as a function of q_z. Shown are the traces for the (a) fundamental, (b) second harmonic, and (c) third harmonic CAP modes under the assumption of a perfect crystal lattice (P.L.) as well as for the case of a slightly distorted crystal lattice (D.L.). (d) Central part of the relrod profile at maximum atomic displacement field, calculated for the fundamental and first two higher-order CAP modes. The reference distribution (dashed line, no CAP mode active) can be used to compare the location q_z where the Ewald sphere intersects the relrod. The change in relrod distribution is magnified here to illustrate the effect of individual CAP modes more clearly.

transient (Figure 6c). For the $3f_1$ component, the analysis yields a phase of 0 or 180° for all values of q_z, whereas a phase of ±90° is obtained for the $6f_1$ component (Figure 7c).

In case of the second harmonic CAP mode, the average interatomic distance in the membranes' out-of-plane direction is not altered because of the symmetric atomic displacement associated with even-order modes. Accordingly, the center of the corresponding relrod profile is not shifted in reciprocal space. Still, the UED technique is sensitive to these modes, with the intensity modulation originating from the redistribution of the relrod profile in the presence of the atomic displacement field.

Assuming a perfect crystal lattice, as we have done so far, the numerical analysis for the second harmonic CAP mode yields an intensity modulation with frequency $4f_1$, whereas the frequency $2f_1$ of the actual atomic vibration is not contained in the transient (Figure 6b, first half-period). Nevertheless, this frequency was observed in the double-pulse experiment adjusted for constructive interference with the second harmonic CAP mode. Moreover, in the double-pulse experiment, the phase of the $2f_1$ contribution with respect to the residual fundamental was found to be significantly different from the one that was obtained for the $2f_1$ frequency component in the single-pulse measurement.

Therefore, in an attempt to refine the model to better capture imperfect experimental conditions, we consider the presence of a small asymmetric lattice distortion in the crystals' out-of-plane direction. In addition to the effect of surface atom relaxation in a nanofilm,[42] this assumption is reasonable because in the experiment, the crystal flake is slightly bulging into the meshes of the supporting copper grid. Although this bulging leads to in-plane lattice distortions as well, we assume that the lattice distortion parallel to the propagation direction of longitudinal CAPs has the dominant influence on the sensitivity to specific modes. Furthermore, besides the mentioned aspects, the sample comes into contact with

https://doi.org/10.1021/acs.jpcc.2c06401
J. Phys. Chem. C 2022, 126, 19822−19833

different chemicals on the upper and lower surfaces during the preparation process, so that an effective asymmetric surface stress could be considered.

Using a third-order polynomial (centered in the middle of the atomic chain) as a proof-of-principle approach to model the assumed lattice distortion, the numerical analysis reproduces the experimentally observed $2f_1$ frequency contribution (Figure 6b, second half-period) with a phase of 0 or 180° with respect to the fundamental, depending on the intersection point q_z (Figure 7b). If one additionally considers the superposition of the two temporally delayed excitation pulses in the double-pulse experiment, this leads to an expected phase of 0 or 180° between the $2f_1$ frequency (originating from the second harmonic CAP mode) and the f_1 frequency (originating from the residual fundamental CAP mode). This phase relationship is therefore different from the expected ±90° relative phase between the f_1 and $2f_1$ frequency contributions in the presence of the fundamental CAP mode.

The comparison of the calculated phases with the experimental results now helps us to identify the measured $2f_1$ frequency contribution in the single-pulse experiment mainly as an effect inherent to the UED measurement principle. Since the experimentally obtained relative phase of −118° with respect to the fundamental frequency f_1 tends toward −90°, we assume that the $2f_1$ contribution predominantly originates from the nonlinear relationship between the observed change in the diffracted intensity and the displacement field amplitude. However, a superimposed smaller contribution from the second harmonic CAP mode possibly exists as well and could explain the deviation from the calculation.

In contrast, for the double-pulse measurement in constructive interference with the second harmonic CAP mode, the measured relative phase was determined to be 18°. This is close to the expected phase in the presence of the second harmonic CAP mode under the assumption of a small asymmetric lattice distortion. Similarly, for the double-pulse experiment in constructive interference with the third harmonic CAP mode, the fitted relative phase of −198° is close to the expected value obtained from the numerical analysis. These conclusions are additionally supported, when the strongly attenuated fundamental in the double-pulse experiment is considered, which most likely rules out the possibility that the observed higher-order frequencies originate from the nonlinear effects described above. Moreover, since the numerical analysis does not show a significant $3f_1$ component in the presence of the fundamental or the second harmonic mode, this additionally strengthens the assignment of the experimental observation of the $3f_1$ frequency contribution to the third harmonic CAP mode.

CONCLUSIONS

In this study, we addressed the question of whether it is possible to excite and amplify higher harmonic CAP modes in thin (few 10 nm-thickness regime) nanofilms employing tailored femtosecond laser excitation schemes. As a prototypical van der Waals material, a ∼42 nm quasi-freestanding graphite membrane was used as a model system. Our UED measurements demonstrate that the first two higher harmonic CAP modes can be driven selectively in a coherent fashion using double-pulse excitation sequences in constructive interference with the respective CAP harmonic. This expands on previous studies on laser-excited CAPs in nanofilms, which revealed a strong discrepancy in the measured spectrum of higher-order CAP modes in thinner and thicker (few 100 nm-thickness regime) specimen. While higher harmonics are often clearly present in thicker films, they are absent or only faintly visible in measurements on thinner films. Therefore, our findings open the way for future experiments employing longer pulse trains or even more complex pulse shapes in order to amplify and manipulate the spectrum of higher harmonic CAP modes in a desired manner for nanofilms in the investigated thickness regime. We note that although the results presented in this work are discussed within the framework of the UED technique, a transfer of the main findings to other experimental techniques, such as all-optical time-resolved reflectometry, is in principle possible.

AUTHOR INFORMATION

Corresponding Authors

Arne Ungeheuer − *Institut für Physik, Universität Kassel, 34132 Kassel, Germany;* orcid.org/0000-0002-0021-8689; Email: arne.ungeheuer@physik.uni-kassel.de

Arne Senftleben − *Institut für Physik, Universität Kassel, 34132 Kassel, Germany;* orcid.org/0000-0003-0932-9892; Email: arne.senftleben@uni-kassel.de

Authors

Ahmed S. Hassanien − *Institut für Physik, Universität Kassel, 34132 Kassel, Germany*

Mashood T. Mir − *Institut für Physik, Universität Kassel, 34132 Kassel, Germany*

Lukas Nöding − *Institut für Physik, Universität Kassel, 34132 Kassel, Germany*

Thomas Baumert − *Institut für Physik, Universität Kassel, 34132 Kassel, Germany*

Complete contact information is available at: https://pubs.acs.org/10.1021/acs.jpcc.2c06401

Author Contributions

The manuscript was written through contributions of all authors. All authors have given approval to the final version of the manuscript.

Notes

The authors declare no competing financial interest.

REFERENCES

(1) Faria, J. C. D.; Garnier, P.; Devos, A. Non-Destructive Spatial Characterization of Buried Interfaces in Multilayer Stacks via Two Color Picosecond Acoustics. *Appl. Phys. Lett.* **2017**, *111*, 243105.

(2) Grossmann, M.; Schubert, M.; He, C.; Brick, D.; Scheer, E.; Hettich, M.; Gusev, V.; Dekorsy, T. Characterization of Thin-Film Adhesion and Phonon Lifetimes in Al/Si Membranes by Picosecond Ultrasonics. *New J. Phys.* **2017**, *19*, No. 053019.

(3) Rossignol, C.; Chigarev, N.; Ducousso, M.; Audoin, B.; Forget, G.; Guillemot, F.; Durrieu, M. C. In Vitro Picosecond Ultrasonics in a Single Cell. *Appl. Phys. Lett.* **2008**, *93*, 123901.

(4) Danworaphong, S.; Tomoda, M.; Matsumoto, Y.; Matsuda, O.; Ohashi, T.; Watanabe, H.; Nagayama, M.; Gohara, K.; Otsuka, P. H.; Wright, O. B. Three-Dimensional Imaging of Biological Cells with Picosecond Ultrasonics. *Appl. Phys. Lett.* **2015**, *106*, 163701.

(5) Scherbakov, A. V.; Salasyuk, A. S.; Akimov, A. V.; Liu, X.; Bombeck, M.; Brüggemann, C.; Yakovlev, D. R.; Sapega, V. F.; Furdyna, J. K.; Bayer, M. Coherent Magnetization Precession in Ferromagnetic (Ga,Mn)As Induced by Picosecond Acoustic Pulses. *Phys. Rev. Lett.* **2010**, *105*, No. 117204.

(6) Kim, J.-W.; Vomir, M.; Bigot, J.-Y. Ultrafast Magnetoacoustics in Nickel Films. *Phys. Rev. Lett.* **2012**, *109*, No. 166601.
(7) Novoselov, K. S.; Geim, A. K.; Morozov, S. V.; Jiang, D.; Zhang, Y.; Dubonos, S. V.; Grigorieva, I. V.; Firsov, A. A. Electric Field Effect in Atomically Thin Carbon Films. *Science* **2004**, *306*, 666−669.
(8) Novoselov, K. S.; Jiang, D.; Schedin, F.; Booth, T. J.; Khotkevich, V. V.; Morozov, S. V.; Geim, A. K. Two-Dimensional Atomic Crystals. *Proc. Natl. Acad. Sci. U. S. A.* **2005**, *102*, 10451−10453.
(9) Nicoul, M.; Shymanovich, U.; Tarasevitch, A.; Linde, D. v. d.; Sokolowski-Tinten, K. Picosecond Acoustic Response of a Laser-Heated Gold-Film Studied with Time-Resolved X-Ray Diffraction. *Appl. Phys. Lett.* **2011**, *98*, 191902.
(10) Wang, X.; Li, J.; Cao, J. Coherent Phonon Generation in Laser-Heated Gold Nanofilm. *J. Chem. Phys.* **2020**, *152*, 124704.
(11) Bugayev, A.; Esmail, A.; Abdel-Fattah, M.; Elsayed-Ali, H. E. Coherent Phonons in Bismuth Film Observed by Ultrafast Electron Diffraction. *AIP Adv.* **2011**, *1*, No. 012117.
(12) Nie, S.; Wang, X.; Li, J.; Clinite, R.; Cao, J. Femtosecond Electron Diffraction: Direct Probe of Ultrafast Structural Dynamics in Metal Films. *Microsc. Res. Tech.* **2009**, *72*, 131−143.
(13) Chatelain, R. P.; Morrison, V. R.; Klarenaar, B. L. M.; Siwick, B. J. Coherent and Incoherent Electron-Phonon Coupling in Graphite Observed with Radio-Frequency Compressed Ultrafast Electron Diffraction. *Phys. Rev. Lett.* **2014**, *113*, No. 235502.
(14) Ge, S.; Liu, X.; Qiao, X.; Wang, Q.; Xu, Z.; Qiu, J.; Tan, P.-H.; Zhao, J.; Sun, D. Coherent Longitudinal Acoustic Phonon Approaching THz Frequency in Multilayer Molybdenum Disulphide. *Sci. Rep.* **2014**, *4*, 5722.
(15) Jeong, T. Y.; Jin, B. M.; Rhim, S. H.; Debbichi, L.; Park, J.; Jang, Y. D.; Lee, H. R.; Chae, D.-H.; Lee, D.; Kim, Y.-H.; et al. Coherent Lattice Vibrations in Mono- and Few-Layer WSe_2. *ACS Nano* **2016**, *10*, 5560−5566.
(16) Huang, Y.-K.; Chern, G.-W.; Sun, C.-K.; Smorchkova, Y.; Keller, S.; Mishra, U.; DenBaars, S. P. Generation of Coherent Acoustic Phonons in Strained GaN Thin Films. *Appl. Phys. Lett.* **2001**, *79*, 3361−3363.
(17) Miao, X.; Zhang, G.; Wang, F.; Yan, H.; Ji, M. Layer-Dependent Ultrafast Carrier and Coherent Phonon Dynamics in Black Phosphorus. *Nano Lett.* **2018**, *18*, 3053−3059.
(18) Glinka, Y. D.; Babakiray, S.; Johnson, T. A.; Holcomb, M. B.; Lederman, D. Acoustic Phonon Dynamics in Thin-Films of the Topological Insulator Bi_2Se_3. *J. Appl. Phys.* **2015**, *117*, 165703.
(19) Hudert, F.; Bruchhausen, A.; Issenmann, D.; Schecker, O.; Waitz, R.; Erbe, A.; Scheer, E.; Dekorsy, T.; Mlayah, A.; Huntzinger, J.-R. Confined Longitudinal Acoustic Phonon Modes in Free-Standing Si Membranes Coherently Excited by Femtosecond Laser Pulses. *Phys. Rev. B* **2009**, *79*, No. 201307.
(20) Schubert, M.; Grossmann, M.; He, C.; Brick, D.; Scheel, P.; Ristow, O.; Gusev, V.; Dekorsy, T. Generation and Detection of Gigahertz Acoustic Oscillations in Thin Membranes. *Ultrasonics* **2015**, *56*, 109−115.
(21) Harb, M.; Peng, W.; Sciaini, G.; Hebeisen, C. T.; Ernstorfer, R.; Eriksson, M. A.; Lagally, M. G.; Kruglik, S. G.; Miller, R. J. D. Excitation of Longitudinal and Transverse Coherent Acoustic Phonons in Nanometer Free-Standing Films of (001) Si. *Phys. Rev. B* **2009**, *79*, No. 094301.
(22) Wu, S.; Lu, Z.; Hu, A.; Miao, X.; Wang, F.; Sun, Z.; Yan, H.; Zhang, H.; Ji, M. Dichroic Photoelasticity in Black Phosphorus Revealed by Ultrafast Coherent Phonon Dynamics. *J. Phys. Chem. Lett.* **2021**, *12*, 5871−5878.
(23) Gerbig, C.; Senftleben, A.; Morgenstern, S.; Sarpe, C.; Baumert, T. Spatio-Temporal Resolution Studies on a Highly Compact Ultrafast Electron Diffractometer. *New J. Phys.* **2015**, *17*, No. 043050.
(24) Thomas, G.; Bell, W. L.; Otte, H. M. Interpretation of Electron Diffraction Patterns from Thin Platelets. *Phys. Status Solidi B* **1965**, *12*, 353−366.
(25) Castellanos-Gomez, A.; Buscema, M.; Molenaar, R.; Singh, V.; Janssen, L.; van der Zant, H. S. J.; Steele, G. A. Deterministic Transfer of Two-Dimensional Materials by All-Dry Viscoelastic Stamping. *2D Mater.* **2014**, *1*, No. 011002.
(26) Yeh, P.; Hendry, M. Optical Waves in Layered Media. *Phys. Today* **1990**, *43*, 77−78.
(27) Ruan, C.-Y.; Vigliotti, F.; Lobastov, V. A.; Chen, S.; Zewail, A. H. Ultrafast Electron Crystallography: Transient Structures of Molecules, Surfaces, and Phase Transitions. *Proc. Natl. Acad. Sci. U. S. A.* **2004**, *101*, 1123−1128.
(28) Schäfer, S.; Liang, W.; Zewail, A. H. Primary Structural Dynamics in Graphite. *New J. Phys.* **2011**, *13*, No. 063030.
(29) Thomsen, C.; Grahn, H. T.; Maris, H. J.; Tauc, J. Surface Generation and Detection of Phonons by Picosecond Light Pulses. *Phys. Rev. B: Condens. Matter Mater. Phys.* **1986**, *34*, 4129−4138.
(30) Bosak, A.; Krisch, M.; Mohr, M.; Maultzsch, J.; Thomsen, C. Elasticity of Single-Crystalline Graphite: Inelastic X-ray Scattering Study. *Phys. Rev. B* **2007**, *75*, No. 153408.
(31) Wright, O. B.; Gusev, V. E. Ultrafast Generation of Acoustic Waves in Copper. *IEEE Trans. Sonics Ultrason.* **1995**, *42*, 331−338.
(32) Ruello, P.; Gusev, V. E. Physical Mechanisms of Coherent Acoustic Phonons Generation by Ultrafast Laser Action. *Ultrasonics* **2015**, *56*, 21−35.
(33) Pinchover, Y.; Rubinstein, J.*An Introduction to Partial Differential Equations*; Cambridge Univ. Press: Cambridge, 2006.
(34) Anisimov, S. I.; Kapeliovich, B. L.; Perel'man, T. L. Electron Emission from Metal Surfaces Exposed to Ultrashort Laser Pulses. *Zh. Eksp. Teor. Fiz.* **1974**, *66*, 375−377.
(35) Cermak, M.; Perez, N.; Collins, M.; Bahrami, M. Material Properties and Structure of Natural Graphite Sheet. *Sci. Rep.* **2020**, *10*, 18672.
(36) Breusing, M.; Ropers, C.; Elsaesser, T. Ultrafast Carrier Dynamics in Graphite. *Phys. Rev. Lett.* **2009**, *102*, No. 086809.
(37) Gierz, I.; Petersen, J. C.; Mitrano, M.; Cacho, C.; Turcu, I. C. E.; Springate, E.; Stöhr, A.; Köhler, A.; Starke, U.; Cavalleri, A. Snapshots of Non-Equilibrium Dirac Carrier Distributions in Graphene. *Nat. Mater.* **2013**, *12*, 1119−1124.
(38) Rohde, G.; Stange, A.; Müller, A.; Behrendt, M.; Oloff, L.-P.; Hanff, K.; Albert, T. J.; Hein, P.; Rossnagel, K.; Bauer, M. Ultrafast Formation of a Fermi-Dirac Distributed Electron Gas. *Phys. Rev. Lett.* **2018**, *121*, No. 256401.
(39) Voisin, C.; Del Fatti, N.; Christofilos, D.; Vallée, F. Time-Resolved Investigation of the Vibrational Dynamics of Metal Nanoparticles. *Appl. Surf. Sci.* **2000**, *164*, 131−139.
(40) Kampfrath, T.; Perfetti, L.; Schapper, F.; Frischkorn, C.; Wolf, M. Strongly Coupled Optical Phonons in the Ultrafast Dynamics of the Electronic Energy and Current relaxation in graphite. *Phys. Rev. Lett.* **2005**, *95*, No. 187403.
(41) Williams, D. B.; Carter, C. B.*Transmission Electron Microscopy: A Textbook for Materials Science*; Springer: New York, 2009.
(42) Sun, C. T.; Zhang, H. Size-Dependent Elastic Moduli of Platelike Nanomaterials. *J. Appl. Phys.* **2003**, *93*, 1212−1218.

https://doi.org/10.1021/acs.jpcc.2c06401
J. Phys. Chem. C 2022, 126, 19822−19833